photonics

MDPI

Article

Multidimensional Optimization of Radio-over-Fiber Links Based on Tunable Carrier-to-Sideband Ratio

Weile Zhai, Jinyuan Ye, Ruihao Wang, Zhong'ao Yang, Jiajun Tan, Xiaoyan Pang, Wanzhao Cui and Yongsheng Gao *

School of Electronics and Information, Northwestern Polytechnical University, Xi'an 710129, China
* Correspondence: ysgao@nwpu.edu.cn

Abstract

In radio-over-fiber (RoF) links, optical single-sideband (OSSB) modulation is an effective method to mitigate power fading caused by chromatic dispersion. However, its low modulation efficiency leads to suboptimal link performance. To address this, we propose a tunable optical carrier-to-sideband ratio (OCSR) OSSB modulation scheme based on a dual-electrode Mach–Zehnder modulator (DEMZM) in a Sagnac loop. Firstly, by adjusting the OCSR, higher radio-frequency (RF) transmission efficiency can be achieved. The experimental results demonstrate that the proposed link provides a 6 dB improvement in received RF power compared to conventional SSB modulation schemes. Furthermore, this approach effectively optimizes nonlinear distortions in the link, achieving a 12.14 dB enhancement in spurious-free dynamic range (SFDR). For tests conducted with a broadband signal featuring a 15 GHz carrier frequency and 500 MHz bandwidth, the optimal error vector magnitude (EVM) reaches 4.88%. Additionally, the link performance can be flexibly improved by adjusting the polarization controller configurations for each channel, making it suitable for multi-user application scenarios.

Keywords: radio over fiber; optical single sideband (OSSB); tunable carrier-to-sideband ratio; link gain; linearization

1. Introduction

Compared to coaxial analog links, radio-over-fiber (RoF) technology offers broader application prospects due to its advantages of low loss, large bandwidth, and immunity to electromagnetic interference. It has been widely adopted in various fields such as broadband wireless access networks, sensor networks, radar systems, satellite communications, and combat systems [1–3]. In RoF transmission links, the primary modulation schemes include double-sideband (DSB) modulation, single-sideband (SSB) modulation, and carrier-suppressed modulation [4–6]. Considering system complexity and modulation efficiency, DSB modulation is the most commonly used method. However, DSB-modulated signals are susceptible to periodic power fading caused by fiber chromatic dispersion [7–9]. This issue can be mitigated by SSB modulation, which also offers the advantage of high spectral efficiency. Nevertheless, in optical single-sideband (OSSB) modulation, since one optical sideband is suppressed, it results in a loss of half the radio-frequency (RF) signal power compared to DSB modulation, leading to lower modulation efficiency and adversely affecting link performance. To optimize this limitation and improve RF modulation efficiency, C. Lim et al. proposed and investigated the concept of the optical carrier-to-sideband ratio (OCSR) to enhance RoF link performance [10]. OCSR is a factor related to the modulation

Check for updates

Received: 13 May 2026
Revised: 11 June 2026
Accepted: 17 June 2026
Published: 21 June 2026

Copyright: © 2026 by the authors. Licensee MDPI, Basel, Switzerland. This article is an open access article distributed under the terms and conditions of the Creative Commons Attribution (CC BY) license.

index. When the modulator is driven by RF signals with different amplitudes, the modulation index changes, thereby altering the OCSR. In reference [10], a fiber Bragg grating (FBG) was used to achieve several specific discrete OCSR values. Their results indicated that a 0 dB OCSR is the optimal point for link performance. However, this configuration does not allow continuous tuning of the OCSR. In addition, multimode optical fibers have gradually gained attention in short-distance wireless access systems due to their low cost and large core diameter. The effects of inter-mode dispersion and differential mode delay on the performance of RoF links have been extensively studied. This includes low-noise RoF transmission in gradient-index plastic optical fibers [11,12], theoretical analysis of bandwidth characteristics of multimode step-index photonic crystal fibers [13], balanced mode distribution and steady-state distribution in core-diameter step-index optical fibers [14], etc. However, the applicability of linearization schemes based on OSSB and tunable OCSR in multimode fibers still lacks systematic research, which is the extended direction discussed in this paper.

For RoF link performance, linearity optimization serves as another core approach for enhancement, playing a significant role in improving the spurious-free dynamic range (SFDR). SFDR reflects the link's ability to handle both weak and strong signals simultaneously, and its performance directly determines the system's anti-interference capability and multi-carrier support capacity, making it particularly critical in multi-band, high-density modulation scenarios. Apart from the non-linear distortions inherent in lasers and photodetectors, which are difficult to quantify, the primary non-linear components generated during modulation originate from the sinusoidal transfer function of the intensity modulator. In sub-octave systems, third-order intermodulation distortion (IMD3) is regarded as the main limiting distortion factor [15]. To improve the linearity of RoF links, electronic methods such as pre-distortion [16], feedforward [17], and digital signal processing [18] have been proposed. However, these methods are constrained by the electronic bottleneck. Links based on parallel modulators [19,20] have achieved the cancelation of both origins of IMD3, but the dual-parallel Mach–Zehnder modulator (DPMZM) requires precise control of three DC biases and needs bias control circuits to prevent bias drift. A linearized link using a polarization modulator (PolM) in a Sagnac loop was proposed in [21], where distortion was reduced by controlling the power ratio and phase difference of the split signals. Subsequently, in [22], an SFDR improvement of 10.3 dB was realized in a Sagnac loop. In summary, since the optimal OCSR and intermodulation distortion suppression generally cannot be achieved simultaneously, multidimensional optimization of RoF links requires a holistic consideration of both OCSR optimization and IMD3 suppression. Therefore, achieving tunable OCSR in RoF links is of great importance. In [23], an OSSB scheme with tunable OCSR based on a DPMZM was proposed. By adjusting the bias voltage of the DPMZM, a wide range of OCSR tunability was obtained. The effect of OCSR on IMD3 was experimentally tested; however, since OCSR was adjusted by varying the modulator bias voltage, this method cannot adapt to multi-base station transmission scenarios, significantly reducing system flexibility and scalability. Later, in [24], an OSSB method using cascaded PolMs was reported. By adjusting the polarization direction of the polarizer, an OSSB-modulated signal with tunable OCSR was generated. This method achieved a large OCSR tuning range covering 5–35 GHz with high flexibility, but the use of two PolMs substantially increases cost. Other structures based on integrated polarization-division multiplexing Mach–Zehnder modulators (PDM-MZM) [25] or Sagnac loops [26] can also be used to adjust OCSR.

In this paper, we propose an OSSB link scheme with tunable OCSR based on a dual-electrode Mach–Zehnder modulator (DEMZM) in a Sagnac loop. The proposed configuration achieves wide-range OCSR tuning and has been tested for vector signal applications.

https://doi.org/10.3390/photonics13060600

This structure enables independent tuning of multiple channels under a shared modulator, meeting multi-channel application requirements with a flexible and simplified architecture. Additionally, it can be utilized for IMD3 suppression, achieving a 12.14 dB improvement in SFDR compared to conventional SSB links. For tests conducted with a broadband signal featuring a 15 GHz carrier frequency, 500 MHz bandwidth, and 10 dBm input power, the optimal error vector magnitude (EVM) reaches 4.88%. Section 2 introduces the principles and theoretical models. Section 3 focuses on the experiments and results and we present the discussion in Section 4. Section 5 provides the research conclusion.

2. Principles and Theoretical Models

Under traditional modulation methods, RoF links encounter issues such as periodic power fading caused by fiber dispersion and spurious distortion resulting from the non-linearity of devices like modulators. These problems simultaneously affect key indicators of the link, including the signal-to-noise ratio, system gain, and spurious-free dynamic range, thereby deteriorating the overall performance of the link. Single-sideband modulation can suppress the problem of periodic power attenuation caused by fiber dispersion. However, it still faces severe modulation non-linear distortion problems. The OCSR tuning technology can precisely address the inter-modulation distortion problem and optimize the system gain. Consequently, we propose an OCSR tuning optimization method based on SSB modulation. Through this scheme, while maintaining the anti-fading advantage of the OSSB, we can achieve the joint optimization of link gain and non-linear performance. The link structure of the proposed scheme is shown in Figure 1. Intuitively, we achieve polarization multiplexing of the optical carrier by adjusting polarization controller 1 (PC1), realize OSSB modulation by adjusting the bias point of the DEMZM, and implement OCSR tuning by controlling PC3, thus solving the problems discussed above. The specific structure of the overall link and the theoretical principles of each part will be elaborated in the following three sub-sections.

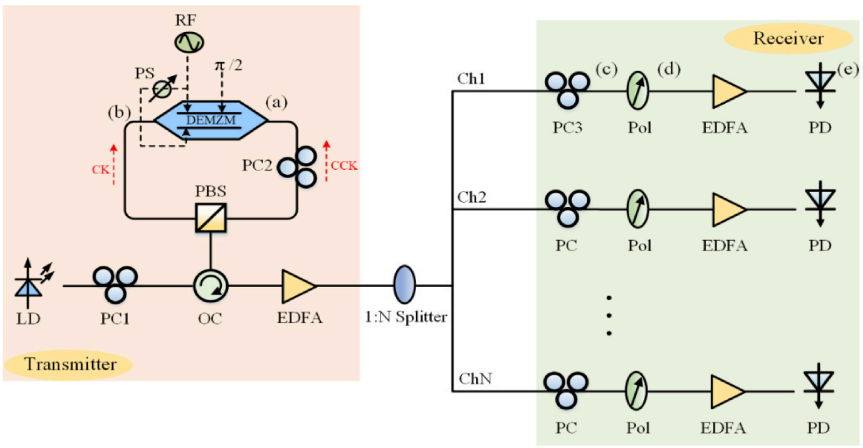


Figure 1. Structure of the multi-channel triple-function RoF system based on OSSB. LD: laser diode, PC: polarization controller, EDFA: erbium-doped fiber amplifier, Pol: polarizer, PD: photodetector.

2.1. The Modulation Principle of OSSB and Its Mechanism for Suppressing Periodic Power Fading

In conventional intensity modulation direct detection (IMDD) links, the chromatic dispersion of optical fiber introduces periodic power fading in the output RF signal. Taking the small-signal DSB modulation of a conventional Mach–Zehnder modulator (MZM) as an example, the output optical signal after transmission over a segment of single-mode fiber can be expressed as Equation (1). This section first introduces the basic principle of

OSSB modulation. In the subsequent Section 2.2, an optical single-sideband modulation scheme with tunable OCSR will be proposed.

$$E_{SMF}(t) \propto \begin{bmatrix} J_1(m)\exp j(\omega_c t + \omega_{RF} t + 3\pi/4 + \theta_1) + \\ J_0(m)\exp j(\omega_c t + \pi/4 + \theta_0) + \\ J_1(m)\exp(\omega_c t - j\omega_{RF} t + 3\pi/4 + \theta_{-1}) \end{bmatrix} \quad (1)$$

In this equation, θ_0, θ_1 and θ_{-1} respectively represent the phase shifts introduced by fiber dispersion to the optical carrier, the +1st-order sideband, and the −1st-order sideband [27].

$$\begin{aligned} \theta_0 &= L\beta(\omega_c) \\ \theta_{\pm 1} &= L\beta(\omega_c) \pm \tau_c\omega_s + \tfrac{1}{2}D{\omega_s}^2 \end{aligned} \quad (2)$$

In this equation, τ and D represent the group delay experienced by the optical carrier and the first-order dispersion coefficient after transmission over a fiber of length L, respectively. After photodetection, considering only the fundamental frequency component at the output, the resulting photocurrent can be expressed as:

$$\begin{aligned} i(t) &= E_{SMF}(t) \cdot E_{SMF}(t)^* \\ &= J_0(m)J_1(m)[\sin(\omega_s t + \theta_1 - \theta_0) - \sin(\omega_s t - \theta_{-1} + \theta_0)] \end{aligned} \quad (3)$$

Substituting Equation (2) into Equation (3) yields:

$$i(t) = 2\sin(\frac{D\omega_s^2}{2})\cos(\omega_s t + \tau(\omega_s)) \quad (4)$$

As observed, the first-order dispersion coefficient D is the primary cause of periodic power fading. In DSB modulation, fiber dispersion introduces different phase shifts to each optical sideband. Thus, during photodetection, these signals interfere, converting the relative phase variations into amplitude fluctuations of the output RF signal, thereby resulting in power fading. From Equation (4), it can be seen that the amplitude of the output radio-frequency current is proportional to $\left|2sin\left(\frac{D\omega_s^2}{2}\right)\right|$. This indicates that as the angular radio frequency changes, the radio frequency power will exhibit oscillatory attenuation. When $\frac{D\omega_s^2}{2} = k\pi$ (k is an integer), the output power reaches zero, and the frequency intervals between adjacent zeros constitute a periodic behavior. This phenomenon is known as "periodic power fading". OSSB modulation retains only one sideband, eliminating the phase difference between two sidebands due to dispersion. In this case, the photodetector detects only the interference between the carrier and a single sideband. As a result, the destructive interference between sidebands is avoided, leading to effective suppression of periodic fading.

2.2. The Principle of Tunable OCSR and Its Mechanism for Enhancing System Gain

Figure 1 shows the structure of the multi-channel RoF system with tunable OCSR based on OSSB modulation. The system consists of a laser diode (LD), polarization controllers (PCs), an optical circulator (OC), a polarization beam splitter (PBS), a dual-electrode Mach–Zehnder modulator (DEMZM), an erbium-doped fiber amplifier (EDFA), a polarizer (Pol), and a photodetector (PD). The optical carrier from the LD is transmitted through PC1 and the OC into the Sagnac loop.

The optical field emitted by the LD is expressed as $E_{in} = E_0 exp(j\omega_c t)$, where E_0 is the amplitude of the optical carrier and ω_0 is the angular frequency. By adjusting PC1, the optical carrier is split by the PBS into two linearly polarized beams with equal power and orthogonal polarization states. We define the polarization state of the clockwise (CK) signal from PBS port 1 as X, and that of the counter-clockwise (CCK) signal from port 2 as

Y. Orthogonal RF signals with a 90° phase shift are applied to the upper and lower arms of the DEMZM. The RF signal can be expressed as $V_{RF} = V_{RF}\cos(\omega_{RF}t)$, where V_{RF} is the amplitude and ω_{RF} is the angular frequency. The modulation index (MI) of the RF signal is given by $m = \pi V_{RF}/V_{\pi}$, where V_{π} is the half-wave voltage of the modulator. Since the DEMZM is a traveling-wave modulator, the optical signal entering in the clockwise direction is modulated, while the signal entering in the counter-clockwise direction remains largely unmodulated. When the DEMZM is biased at the quadrature transmission point, OSSB modulation is achieved for the clockwise signal. The optical signal at the output (a) of the modulator can be expressed as:

$$E_{CK}(t) = \sqrt{\mu/2}E_{in}(t)\begin{bmatrix} (1-j)J_0(m_{RF}) \\ +2J_{-1}(m_{RF})\exp(-j\omega_{RF}t) \end{bmatrix} \quad (5)$$

Here, μ represents the insertion loss of the DEMZM, and $Jn(.)$ is the nth-order Bessel function of the first kind. When the MI is small, the higher-order optical sidebands in Equation (1) can be neglected, which corresponds to the optical spectrum (a) in Figure 2.

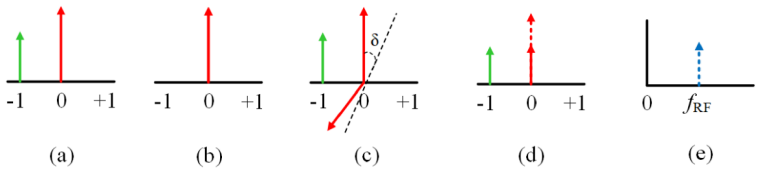


Figure 2. Spectrogram of key nodes of the proposed link.

The CCK optical carrier undergoes negligible modulation and can therefore be disregarded. Thus, the optical signal at the modulator output (b) can be expressed as:

$$E_{CCK}(t) = \sqrt{\mu/2}E_{in}(t) \quad (6)$$

This corresponds to the optical spectrum in Figure 2b. The two optical signals then recombine at the PBS, forming a polarization-multiplexed optical signal that is routed out through the OC. PC2 is adjusted to align the polarization state of the CK signal with the principal axis of the PBS. The optical signal output from the Sagnac loop is amplified by an EDFA and then undergoes wavelength division multiplexing. Taking Channel 1 at the receiver side as an example, PC3 controls the polarization state of the polarization-multiplexed signal such that the modulated CK signal forms an angular deviation δ from the principal axis of the polarizer. The CK and CCK optical signals maintain a constant 90° phase difference, meaning they remain in orthogonal polarization states. The signal spectrum before entering the polarizer is shown in Figure 2c, while the optical signal output from the polarizer is depicted in Figure 2d. Note that for simplicity, it is assumed that the signals amplified by the EDFA and multiplexed into each channel do not undergo significant power variations. Thus, the optical signal after the polarizer can be expressed as:

$$\begin{aligned} E_{out}(\mathrm{t}) &= E_{CK}(\mathrm{t})\cos\delta + E_{CCK}(\mathrm{t})\sin\delta \\ &= \sqrt{\mu/2}E_{in}(\mathrm{t})\begin{bmatrix} (1-\mathrm{j})J_0(\mathrm{m})\cos\delta + \sin\delta \\ -2J_1(\mathrm{m})\cos\delta\exp(-\mathrm{j}\omega_{RF}\mathrm{t}) \end{bmatrix} \end{aligned} \quad (7)$$

At this point OCSR can be defined as the power ratio between the optical carrier and the −1st-order sideband, denoted as:

$$OCSR = \left[\left|\frac{(1-\mathrm{j})J_0(\mathrm{m})\cos\delta+\sin\delta}{-2J_1(\mathrm{m})\cos\delta}\right|\right]^2 = \frac{J_0^2(\mathrm{m})}{2J_1^2(\mathrm{m})} + \frac{\tan^2\delta}{4J_1^2(\mathrm{m})} + \frac{J_0(\mathrm{m})\tan\delta}{2J_1^2(\mathrm{m})} \quad (8)$$

From Equation (4), it can be concluded that the OCSR depends on both the modulation index of the DEMZM applied to the clockwise optical carrier and the angle δ between the polarization direction of the modulated optical signal and the principal axis of the polarizer. With the modulation index fixed at m = 0.5, the variation in OCSR with respect to δ is shown in Figure 3. Theoretically, OCSR can be tuned from −30 dB to over 40 dB by adjusting δ.

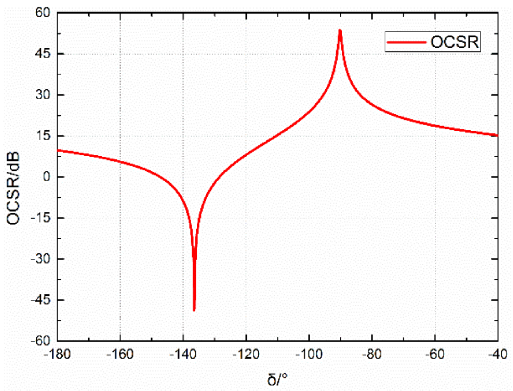


Figure 3. Relationship between the OCSR and the angle δ when m = 0.

Finally, the optical signal is amplified by the EDFA and then converted into an electrical current by the PD. The component of the photocurrent at the angular frequency ω_{RF} can be expressed as:

$$\begin{aligned} i_{\omega_{RF}}(\mathrm{t}) &= \eta|E_{out}(\mathrm{t})|^2_{\omega RF} \\ &= \eta\mu E_0^2|2J_1(\mathrm{m})\cos\delta(J_0(\mathrm{m})\cos\delta+\sin\delta)| \\ &= \eta\mu\sqrt{P_C}\cdot\sqrt{P_S} \end{aligned} \quad (9)$$

where η denotes the responsivity of the PD in A/W. P_C and P_S represent the optical power of the carrier and sideband, respectively. Indeed, using an EDFA to amplify the optical signal in the link can improve system gain. However, since the PD at the receiver end has a limited input saturation power, typically around 10 dBm, it is not feasible to indefinitely increase the optical power input to the PD. When the EDFA is set to Automatic Power Control (APC) mode, the total optical power of the carrier and sideband remains constant. As shown in Equation (9), the amplitude of the RF current after photoelectric detection is proportional to $\sqrt{P_c \cdot P_s}$. That is to say, the RF power is proportional to $\sqrt{P_c \cdot P_s}$. At this time, according to the basic inequality relationship, the power of the carrier and the sideband are equal, that is, $P_C = P_S$, corresponding to OCSR $= 10 \cdot log_{10}(P_c/P_s) = 0$ dB. Therefore, when OCSR = 0 dB, the link RF power is at its maximum. Under this condition, the OCSR further influences the gain performance of the link.

2.3. The Principle of IMD3 Suppression

The system can also be utilized to suppress IMD3, thereby enhancing the linearity of the RoF link. Assuming the DEMZM is driven by a two-tone RF signal with angular frequencies ω_1 and ω_2, the output optical signal in the CK direction can be expressed as:

$$E_X(t) = \sqrt{\mu/2}E_{in}(t)\left[\begin{array}{l}\exp(jm\sin\omega_1 t + jm\sin\omega_2 t) \\ +\exp\left(-jm\sin\omega_1 t - jm\sin\omega_2 t + j\frac{\pi}{2}\right)\end{array}\right] \quad (10)$$

where the modulation index satisfies $m = \pi V_1/V_\pi = \pi V_2/V_\pi$, and the other parameters remain as defined previously. The symbol X denotes the polarization state of the CK signal. The unmodulated optical carrier in the CCK direction can be expressed as:

$$E_Y(t) = \sqrt{\mu/2}E_{in}(t) \tag{11}$$

where the symbol Y represents the polarization state of the CCK signal. After the two signals are combined by the PBS and output via the OC, their components projected onto the principal axis of the polarizer are controlled by the angle δ by adjusting PC3. The X and Y polarization states remain orthogonal throughout this process, with the result illustrated in Figure 4a. Using a Bessel function expansion, the optical field output from the polarizer can be expressed as:

$$\begin{aligned} E_{out}(t) &= E_X(t)\cos\delta + E_Y(t)\sin\delta \\ &= \sqrt{\mu/2}E_0 \left[\begin{array}{l} \sin\delta\exp(j\omega_c t) - \\ (1+j)\cos\delta \sum_{p=-\infty}^{+\infty}\sum_{q=-\infty}^{+\infty} J_p(m)J_q(m) \\ \exp(jp\omega_1 t + jq\omega_2 t) \end{array} \right] \exp(j\omega_c t) \end{aligned} \tag{12}$$

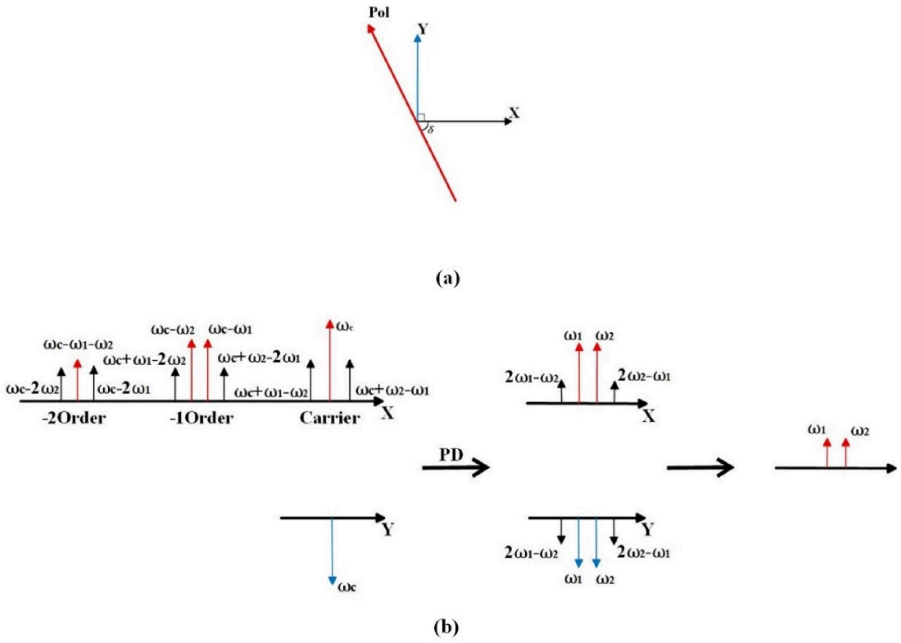


Figure 4. (**a**) Relationship between the X, Y polarization states and the principal axis of the polarizer. (**b**) Optical and electrical spectra illustrating the IMD3 suppression process.

Neglecting higher-order sidebands, the IMD3 component is generated by the beating of three spectral components, namely the optical carrier, the −1st-order optical sideband, and the −2nd-order optical sideband, as illustrated in Figure 4b. After amplification by the EDFA, the signal output from the polarizer is photodetected by the PD. The resulting photocurrent, which includes both the fundamental component and the IMD3 component, is given by:

$$\begin{aligned} i_{AC}(t) &\propto |E_{out}(\mathrm{t})|^2_{AC} \\ &\propto \left(2\sin\delta\cos\delta - 2\cos^2\delta\right) J_0(\mathrm{m}) J_1(\mathrm{m}) \cos(\omega_{1,2}t) \\ &+ \left[\begin{array}{l} 2\sin\delta\cos\delta J_1(\mathrm{m}) J_2(\mathrm{m}) \\ -4\cos^2\delta \left(\begin{array}{l} J_1(\mathrm{m}) J_2(\mathrm{m}) \\ -2J_0(\mathrm{m}) J_1^3(\mathrm{m}) \\ -2J_0^2(\mathrm{m}) J_1(\mathrm{m}) J_2(\mathrm{m}) \end{array} \right) \end{array} \right] \cos(2\omega_{1,2} - \omega_{2,1})\, t \end{aligned} \tag{13}$$

where $\omega_{1,2}$ represents the fundamental RF signals at ω_1 and ω_2, and $2\omega_{1,2} - \omega_{2,1}$ denotes the IMD3. To suppress IMD3 and recover the fundamental signal, the following condition must be satisfied:

$$\sin\delta\cos\delta - \cos^2\delta \neq 0 \tag{14}$$

$$\sin\delta\cos\delta J_1(\mathrm{m}) J_2(\mathrm{m}) - 2\cos^2\delta \left(\begin{array}{l} J_1(\mathrm{m}) J_2(\mathrm{m}) \\ -2J_0(\mathrm{m}) J_1^3(\mathrm{m}) \\ -2J_0^2(\mathrm{m}) J_1(\mathrm{m}) J_2(\mathrm{m}) \end{array} \right) = 0 \tag{15}$$

In practice, satisfying these conditions requires only a minor adjustment of the relevant angle. The optimal angle specified in Equation (15) can be numerically computed using MATLAB (2022b) or equivalent computational tools, yielding a value of $-84.29°$. Therefore, by adjusting PC3 to achieve this optimal δ, the two IMD3 components cancel each other out, leaving only the clean fundamental signal, as shown in Figure 4b.

3. Experiments and Results

The experimental study in this work is divided into three parts. In the first part, a single-tone signal was used to measure the tunable range of the OCSR, and its performance was verified under varying driving signal frequencies. Additionally, the relationship between the output RF power and the OCSR was measured, confirming the impact of OCSR tuning on link gain. The second part involved applying two RF signals to identify the optimal operating point for IMD3 suppression. The SFDR was measured and compared with that of a conventional SSB link, demonstrating the system's capability for linearity optimization. The third part focused on validating the broadband vector signal transmission performance. Using a 4QAM signal as an example, the transmission performance under both low and high input power levels was investigated. The error vector magnitude (EVM) was measured at different OCSR values, proving that dynamic OCSR tuning optimizes both system gain and nonlinear distortion, thereby ensuring high-quality vector signal transmission.

A tunable laser source (Fiber-Photonics TLS-M-C-16-P-FA, USA) was used in the experiment, emitting a continuous-wave optical signal at a wavelength of 1552.2 nm with an optical power of 16 dBm and a linewidth of 20 kHz. The DEMZM (Fujitsu FTM7937EZ200, Japan) had a half-wave voltage of 4.8 V and a bandwidth of 30 GHz. All fiber pigtails in the Sagnac loop were polarization-maintaining, and a PC was integrated into port 2 of the PBS. The optical signal after the polarizer was split into two paths. One path was sent to an optical spectrum analyzer (Finisar WaveAnalyser 15000S, USA), while the other was amplified to 6 dBm by an EDFA (Keyang Photonics KY-EDFA-PA-15-M, China). The PD (GD45220R-C-1, China) had a bandwidth of 33 GHz and a maximum responsivity of 0.75 A/W. The detected signal was then measured using a signal analyzer (Agilent Technologies N9020A, USA). A signal generator (Ceyear 1435F, China) was used to drive the microwave electrodes of the DEMZM. For the two-tone test, an additional RF signal was generated by a microwave analog signal generator (Ceyear 1466G-V, China). DC bias voltages were controlled by a DC power supply (GWINSTEK GPD4303S, Taiwan, China).

3.1. Optimization for Link Gain by Tuning OCSR

In this section, we validate the tunable range of the OCSR and the optimization of link gain through OCSR tuning. In the experiment, a signal generator produces an RF signal at 15 GHz with a power of 10 dBm, which is split into two paths. One path undergoes a 90° phase shift and is applied to the orthogonally biased DEMZM. As derived in the theoretical section, the optical signal in the CK direction undergoes OSSB modulation, while the CCK optical signal remains unmodulated. The corresponding optical spectra are shown in Figure 5a and 5b, respectively. After polarization control, by adjusting PC3, the relative power ratio between the CK and CCK signals after the polarizer is varied, resulting in a tunable OCSR. This enables the generation of an OSSB-modulated signal with adjustable OCSR. The signal is then amplified by an EDFA before being detected by the PD. The resulting optical spectra are shown in Figure 5c and 5d, respectively.

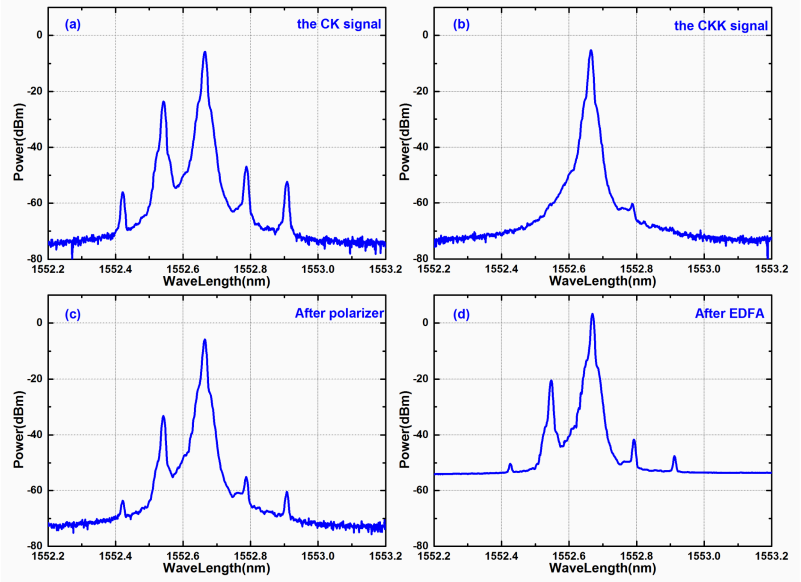


Figure 5. (**a**) Optical spectrum of the CK signal, (**b**) optical spectrum of the CCK signal, (**c**) optical spectrum after the polarizer, and (**d**) optical spectrum after the EDFA.

Figure 6a shows the optical spectra of OSSB signals with different OCSR values at an RF of 15 GHz. The OCSR can be continuously tuned from −30 dB to 20 dB, demonstrating greater flexibility compared to FBG-based OCSR schemes [17]. Figure 6b displays the detailed spectra corresponding to OCSR values of −30 dB and 20 dB. In practice, the OCSR could be tuned from −40 dB to 40 dB in the experiment. However, some spectral configurations were relatively unstable, so only the stable spectra were recorded.

The EDFA was set to operate in APC mode with its output power fixed at 10 dBm. By adjusting the PC to vary the OCSR, the output RF signal power was measured. Figure 7 shows the relationship between the output RF power after PD detection and the OCSR. The RF power initially increases and then decreases as the OCSR increases. The maximum RF power of −8.4 dBm is achieved at an OCSR of 0 dB, which is consistent with the theoretical analysis presented in Section 2.

Furthermore, to verify the system's large operational bandwidth, the RF signal frequency was tuned from 6 GHz to 30 GHz while maintaining an OCSR of 0 dB. The resulting optical spectra are shown in Figure 8, where the sideband power decreases as the input signal frequency increases, indicating a reduction in modulation efficiency at higher frequencies. Since the proposed system achieves tunable OCSR solely by adjusting the PC, the operational bandwidth is limited only by the 90° hybrid coupler or phase shifter. Cur-

rently, commercial phase shifters are available with frequency coverage up to 40 GHz. It should be noted that the inhibitory effect of IMD3 mainly depends on the setting of the polarization angle and is basically independent of the radio frequency. Within the range of 6–30 GHz, as long as the phase error of the 90° hybrid coupler is controlled within ±5°, the OCSR tuning range remains consistent at all tested frequencies. Therefore, the performance of the proposed scheme has good frequency consistency throughout the operating frequency range.

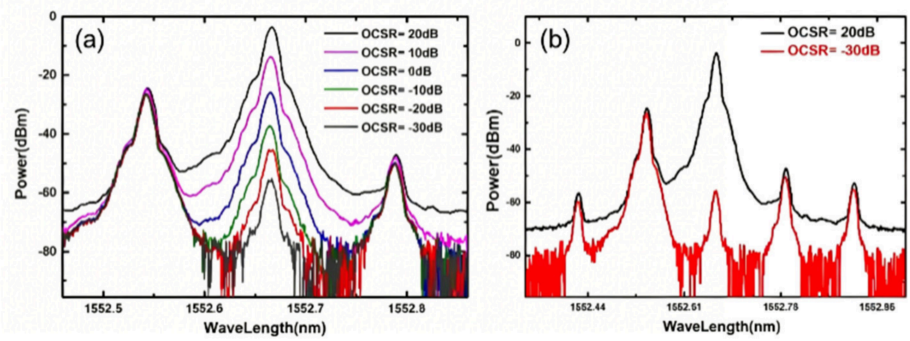


Figure 6. (**a**) Optical spectra of OSSB signals with tunable OCSR. (**b**) Spectra with the maximum OCSR of 20 dB and the minimum OCSR of −30 dB, where the frequency of the driving RF signal is fixed at 15 GHz.

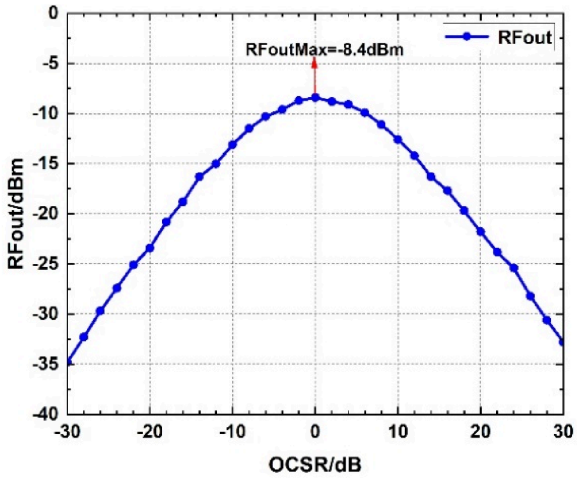


Figure 7. Relationship between output RF power and the OCSR when EDFA operates in APC mode.

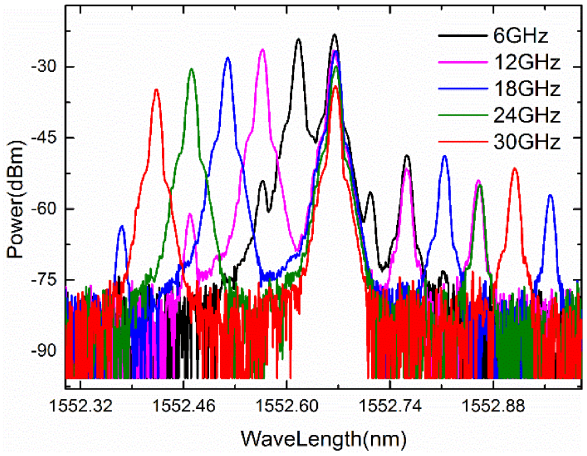


Figure 8. Optical spectra of OSSB-modulated signals with RF frequencies from 6 GHz to 30 GHz.

3.2. Optimization of System Performance with IMD3 Suppression

As derived in the theoretical section, IMD3 can be suppressed by adjusting the polarization state of the polarizer. To evaluate the degree of IMD3 suppression, two RF signals at 15 GHz and 15.01 GHz with a fixed power level of 10 dBm were introduced to the DEMZM via a 90° hybrid coupler. Before linearization optimization, high-power IMD3 components were observed, which severely limited the RoF link performance. By properly adjusting PC3, this nonlinear distortion was partially optimized. The RF spectrum after photodetection was measured, as shown in Figure 9. It can be observed that after optimization via PC3 adjustment, the power ratio between IMD3 and the fundamental RF signal improved from −45 dB to −62 dB, while the fundamental component decreased by only 2 dB.

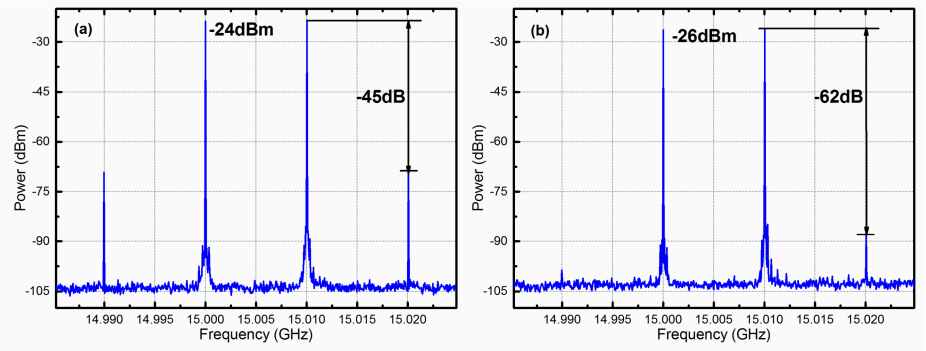


Figure 9. Measured RF spectra (**a**) before optimization and (**b**) after optimization.

In the optimal linearization state, the SFDR of the proposed link is measured and compared with that of a conventional SSB scheme, as shown in Figure 10. The results indicate that the linearized link achieves an SFDR of 108.22 dB·Hz^{2}/^{3}, which is 12.14 dB higher than that of the conventional SSB link. The measured noise floor in the experiment was −136.22 dBm/Hz, limited by amplified spontaneous emission (ASE) noise from the EDFA and noise introduced by the PD. If the noise floor could be controlled at −145 dBm/Hz, the SFDR could be further improved to 117.22 dB·Hz^{2}/^{3}.

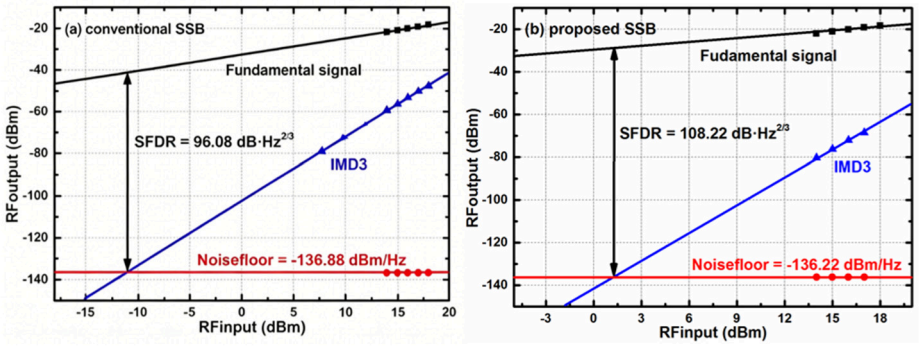


Figure 10. Measured SFDR of (**a**) the conventional SSB link and (**b**) the proposed link.

3.3. Broadband Vector Signal Testing

Next, we employed the same experimental setup to investigate the combined impact of OCSR and IMD3 on the RoF link when transmitting broadband vector signals. The influence of system gain and nonlinear distortion on transmission performance varies with signal power. Under low input power conditions, system gain plays a dominant role, whereas at higher input power levels, nonlinear distortion becomes the primary limiting factor.

To validate the performance improvement achieved by tuning the OCSR, a broadband vector signal with a drive power of 10 dBm and a bandwidth of 500 MHz was used to evaluate the EVM and constellation diagrams at different OCSR values. The results are shown in Figure 11. It can be observed that the EVM degrades as the absolute value of OCSR increases. When the OCSR ranges between −20 dB and 20 dB, the EVM ranges from 4.88% to 28%. This demonstrates that flexible tuning of the OCSR can effectively optimize the EVM performance of the link.

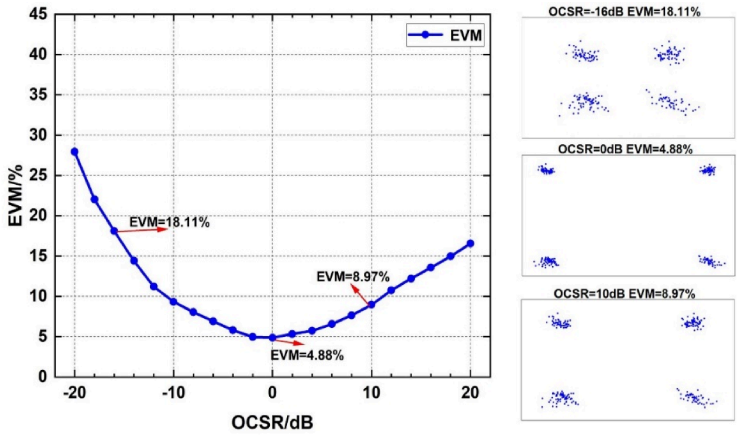


Figure 11. Relationship between EVM and OCSR for 4QAM drive signal with 500 MHz bandwidth, 10 dBm power, and 15 GHz carrier frequency.

Subsequently, to investigate the impact of input power on the transmission performance of 4QAM broadband vector signals in the RoF link, the input power was adjusted from 0 dBm to 20 dBm in 1 dB steps while maintaining the OCSR at 0 dB. The EVM under different input power levels was measured using a signal and spectrum analyzer (Siglent SDS6204 H10 Pro, China), and selected constellation diagrams were recorded. The results are shown in Figure 12. As observed in Figure 12, at lower input power levels, the system exhibits minimal nonlinear distortion. Tuning the OCSR primarily optimizes system gain, resulting in a low EVM after transmission. However, as the input power increases, nonlinear distortion becomes more pronounced, requiring a balanced consideration of both gain and distortion when adjusting the OCSR. Although the proposed scheme cannot simultaneously achieve optimal gain and distortion suppression, the results show a gradual increase in EVM with rising input power. Nevertheless, the system can effectively optimize link performance by tuning the OCSR to balance gain and distortion, thereby minimizing signal quality degradation.

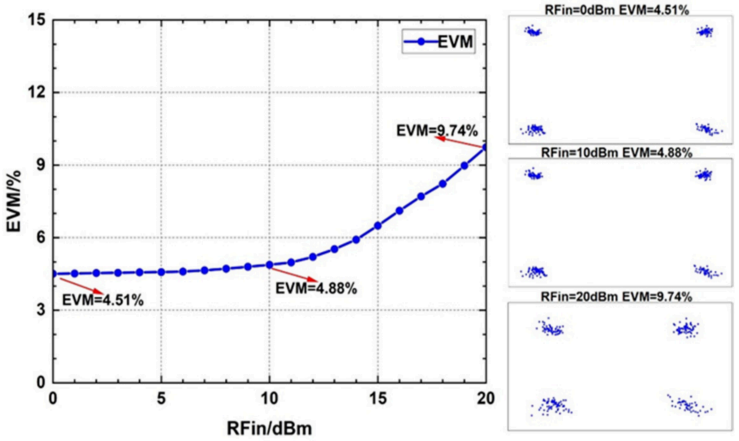


Figure 12. EVM under different input power levels with OCSR fixed at 0 dB.

To further illustrate the performance degradation under high input power, a broadband vector signal with an input power of 20 dBm was used to evaluate the EVM and constellation diagrams at different OCSR values. The results are shown in Figure 13. As can be observed, the EVM still degrades as the absolute value of the OCSR increases. When the OCSR ranges from −20 dB to 20 dB, the EVM varies between 9.12% and 38.65%. It is particularly noteworthy that at this high input power, setting the OCSR to 0 dB no longer yields the optimal EVM, as nonlinear distortion has a more pronounced impact on link performance. The measurements reveal that the best EVM of 9.12% is achieved at an OCSR of −2 dB. Compared with the results in Figure 11, this value is significantly higher than the optimal EVM of 4.88% obtained at a 10 dBm input power.

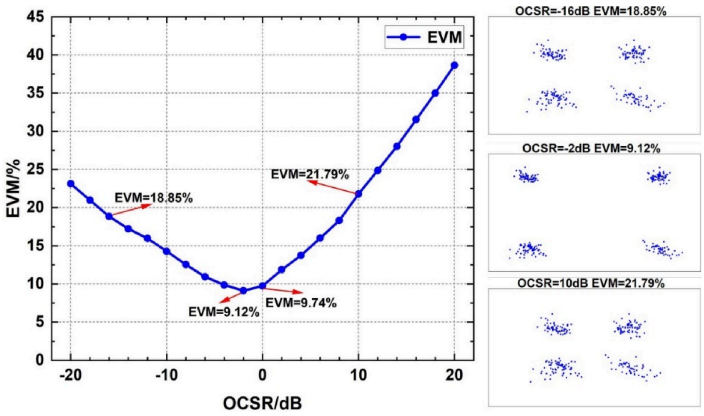


Figure 13. Relationship between EVM and OCSR for 4QAM drive signal with 500 MHz bandwidth, 20 dBm power, and 15 GHz carrier frequency.

4. Discussion

The proposed scheme utilizes OSSB modulation based on a DEMZM within a Sagnac loop. Although the proposed structure is slightly more complex compared to traditional carrier suppression methods, it possesses the following indispensable advantages: compared to the FBG scheme, which is limited by various strict requirements such as laser wavelength, this scheme can achieve continuous and arbitrary tuning; compared with the scheme of bias regulation for electro-optic modulators, the proposed scheme has better flexibility and lower complexity for multi-channel implementation of the system.

However, it should be noted that, in the experiment of the proposed scheme, the method of obtaining the optimal polarization angle based on software calculation is employed to establish an empirical lookup table database. Based on the current input RF power, the target polarization angle can be quickly obtained. And based on the empirical table, by using an electronically controlled polarization controller (Phoenix Photonics EPC, Britain) to replace the traditional three-ring polarization controller, the adjustment of any polarization state can be achieved to determine this optimal polarization angle.

In the face of the polarization change problem caused by environmental disturbances, a polarization control feedback link based on EPC adjustment can be introduced to solve it. The general link structure is shown in Figure 14. The radio-frequency signal output from the original link is transmitted to the EVM/BER measurement module via a coupler. The feedback circuit is driven by an FPGA controller and employs a hill-climbing algorithm to reduce the EVM/BER values, thereby gradually approaching the optimal polarization angle. This allows the EPC to be controlled to stably maintain the target polarization state. In addition, the problem of bias voltage change can also be solved by using a bias voltage controller (PlugTech MBC-IQ-VA, HongKong, China). It can inject a jitter signal into the modulator and adjust the output DC bias voltage to compensate for the drift of the

modulator operating point caused by external environmental changes, thus ensuring good tuning stability of the OCSR.

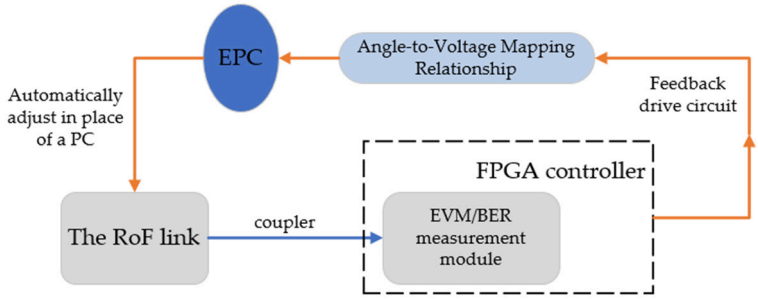


Figure 14. Schematic diagram of the polarization control feedback link based on EPC regulation.

For the Sagnac loop, optical back-reflections from connectors can interfere with the output signal, leading to system instability [28]. This can be mitigated by using connectors with low optical return loss. In our experiment, angled physical contact (APC) connectors were employed to ensure system stability. In the experimental section, the reception performance for both single-tone and vector signals was evaluated. An OCSR of 0 dB was achieved, consistent with theoretical predictions. A two-tone test was also conducted, resulting in an IMD3 suppression ratio of −62 dB. The SFDR was 12.14 dB higher than that of a conventional SSB link. In the current system, the noise floor is mainly limited by the ASE noise of the EDFA. If a balanced detection structure is adopted, common-mode noise can be effectively eliminated, and theoretically, the SFDR can be further improved. Additionally, using photodetectors and preamplifiers with lower noise coefficients can also further reduce distortion. These solutions will be the focus of subsequent work.

5. Conclusions

This paper investigates a novel OSSB modulation scheme with tunable OCSR based on a DEMZM in a Sagnac loop through both theoretical analysis and experimental validation. The proposed scheme significantly optimizes RoF link gain and nonlinear distortion, and enables independent and flexible tuning of multiple channels under a shared modulator. Under the experimental conditions in this work, by adjusting the OCSR to its optimal state, the output RF power is significantly improved to −8.4 dBm, demonstrating superior gain performance compared to conventional SSB modulation. After linearization processing, IMD3 can be effectively suppressed, resulting in a 12.14 dB improvement in SFDR. This indicates the strong potential of the proposed link for use in high-dynamic-range systems. It should be noted that although this paper focuses on the verification of single-channel performance, the proposed architecture can be extended to multiple channels through wavelength division multiplexing. Each receiving end can independently configure the polarization controller and polarizer to achieve independent optimization of the gain and linearity of each user link. Subsequent work will conduct system-level experimental verification in a multi-user and multi-carrier environment to evaluate the inter-user crosstalk and resource scheduling performance.

Author Contributions: Conceptualization, W.Z. and J.Y.; methodology, W.Z. and J.Y.; software, J.Y.; validation, W.Z., J.Y. and R.W.; formal analysis, R.W.; investigation, W.Z., J.Y., R.W., Z.Y., J.T., X.P., W.C. and Y.G.; resources, Y.G.; data curation, J.Y.; writing—original draft preparation, J.Y. and R.W.; writing—review and editing, W.Z.; visualization, W.Z.; supervision, Y.G.; project administration, Y.G.; funding acquisition, Y.G. All authors have read and agreed to the published version of the manuscript.

Funding: This research was funded in part by the National Natural Science Foundation of China under Grant 62301437 and Grant 62171374, in part by the Young Star of Science and Technology Program of Shaanxi under Grant 2023KJXX-133, in part by the Key Research and Development Program of Shaanxi under Grant 2024GX-YBXM-080, in part by Civil Aerospace Technology Pre-research Program (D030301) and in part by ZTE Industry–University–Institute Cooperation Funds under Grant No.IA20250000010.

Institutional Review Board Statement: Not applicable.

Data Availability Statement: Data underlying the results presented in this paper are not publicly available at this time but may be obtained from the authors upon reasonable request.

Conflicts of Interest: The authors declare no conflicts of interest.

References

1. Cox, C. *Analog Optical Links, Theory and Practice*; Cambridge University: Cambridge, UK, 2004.
2. Yao, J.P. Microwave photonics. *J. Light. Technol.* **2009**, *27*, 314–335. [CrossRef]
3. Yuan, J.H.; Fei, Z.S.; Wei, Z.Q. Special Topic on Integrated Sensing and Communication(ISAC) Technologies for Future Wireless Communication. *ZTE Commun.* **2024**, *22*, 1–3. [CrossRef]
4. Jia, Z.; Yu, J.; Chang, G.-K. A full-duplex radio-over-fiber system based on optical carrier suppression and reuse. *IEEE Photon. Technol. Lett.* **2006**, *18*, 1726–1728. [CrossRef]
5. Yu, J.; Jia, Z.; Wang, T.; Chang, G.K. Centralized Lightwave Radio-Over-Fiber System with Photonic Frequency Quadrupling for High-Frequency Millimeter-Wave Generation. *IEEE Photon. Technol. Lett.* **2007**, *19*, 1499–1501. [CrossRef]
6. Park, J.; Sorin, W.; Lau, K. Elimination of the fibre chromatic dispersion penaltyon 1550 nm millimetre-wave optical transmission. *Electron. Lett.* **1997**, *33*, 512–513. [CrossRef]
7. Meslener, G. Chromatic dispersion induced distortion of modulated monochromatic light employing direct detection. *IEEE J. Quantum Electron.* **1984**, *20*, 1208–1216. [CrossRef]
8. Schmuck, H. Comparison of optical millimeter-wave system concepts with regard to chromatic dispersion. *Electron. Lett.* **1995**, *31*, 1848–1849. [CrossRef]
9. Gliese, U.; Norskov, S.; Nielsen, T. Chromatic dispersion in fiber-optic microwave and millimeter-wave links. *IEEE Trans. Microw. Theory Tech.* **1996**, *44*, 1716–1724. [CrossRef]
10. Lim, C.; Attygalle, M.; Nirmalathas, A.; Novak, D.; Waterhouse, R. Analysis of optical carrier-to-sideband ratio for improving transmission performance in fiber-radio links. *IEEE Trans. Microw. Theory Tech.* **2006**, *54*, 2181–2187. [CrossRef]
11. Azusa, I.; Yasuhiro, K. Low-noise radio over graded-index plastic optical fiber. *Opt. Lett.* **2020**, *45*, 3192–3195. [CrossRef] [PubMed]
12. Matsuura, M.; Furukawa, R.; Matsumoto, Y.; Inoue, A.; Koike, Y. Evaluation of modal noise in graded-index silica and plastic optical fiber links for radio over mul-timode fiber systems. *Opt. Express* **2014**, *22*, 6562–6568. [CrossRef] [PubMed]
13. Drljača, B.; Savović, S.; Kovačević, M.S.; Simović, A.; Kuzmanović, L.; Djordjevich, A.; Min, R. Theoretical Investigation of Bandwidth in Multimode Step-Index Silica Photonic Crystal Fibers. *Photonics* **2022**, *9*, 214. [CrossRef]
14. Savović, S.; Djordjevich, A.; Simović, A.; Drljača, B. Equilibrium mode distribution and steady-state distribution in 100–400 μm core step-index silica optical fibers. *Appl. Opt.* **2011**, *50*, 4170–4173. [CrossRef] [PubMed]
15. Marpaung, D.A.I. High Dynamic Range Analog Photonic Links: Designmand Implementation. Ph.D. Thesis, University of Twente, Enschede, The Netherlands, 2009.
16. Childs, R.B.; O'Byme, V.A. Multichannel AM video transmission using a high-power Nd:YAG laser and linearized external modulator. *IEEE J. Sel. Areas Commun.* **1990**, *8*, 1369–1478. [CrossRef]
17. O'Connor, S.R.; Clark, T.R.; Novak, D. Wideband Adaptive Feedforward Photonic Link. *J. Light. Technol.* **2008**, *26*, 2810–2816. [CrossRef]
18. Duan, R.; Xu, K.; Dai, J.; Lv, Q.; Dai, Y.; Wu, J.; Lin, J. Digital linearization technique for IMD3 suppression in intensity-modulated analog optical links. In Proceedings of the 2011 International Topical Meeting on Microwave Photonics jointly held with the 2011 Asia-Pacific Microwave Photonics Conference, Singapore, 18–21 October 2011; pp. 234–237.
19. Li, S.; Zheng, X.; Zhang, H.; Zhou, B. Highly Linear Radio-Over-Fiber System Incorporating a Single-Drive Dual-Parallel Mach–Zehnder Modulator. *IEEE Photon. Technol. Lett.* **2010**, *22*, 1775–1777. [CrossRef]
20. Ferreira, A.; Silveira, T.; Fonseca, D.; Ribeiro, R.; Monteiro, P. Highly Linear Integrated Optical Transmitter for Subcarrier Multiplexed Systems. *IEEE Photon. Technol. Lett.* **2009**, *21*, 438–440. [CrossRef]
21. Li, W.; Wang, L.X.; Zhu, N.H. Highly Linear Microwave Photonic Link Using a Polarization Modulator in a Sagnac Loop. *IEEE Photon. Technol. Lett.* **2013**, *26*, 89–92. [CrossRef]

22. Zhu, W.; Zhao, M.; Fan, F.; Hu, J.; Gu, Y. Sagnac Interferometer-Assisted Microwave Photonic Link with Improved Dynamic Range. *IEEE Photon. J.* **2017**, *9*, 1–9. [CrossRef]
23. Hraimel, B.; Zhang, X.; Pei, Y.; Wu, K.; Liu, T.; Xu, T.; Nie, Q. Optical Single-Sideband Modulation with Tunable Optical Carrier to Sideband Ratio in Radio Over Fiber Systems. *J. Light. Technol.* **2011**, *29*, 775–781. [CrossRef]
24. Zhang, Y.; Zhang, F.; Pan, S. Optical Single Sideband Modulation with Tunable Optical Carrier-to-Sideband Ratio. *IEEE Photon. Technol. Lett.* **2014**, *26*, 653–655. [CrossRef]
25. Gao, Y.; Wen, A.; Peng, Z.; Tu, Z. Analog Photonic Link with Tunable Optical Carrier to Sideband Ratio and Balanced Detection. *IEEE Photon. J.* **2017**, *9*, 1–10. [CrossRef]
26. Wu, B.; Wang, M.; Tang, Y.; Sun, J.; Zhang, J.; Yan, F.; Jian, S. Optical single sideband modulation with tunable optical carrier-to-sideband ratio using a modulator in a Sagnac loop. *Opt. Laser Technol.* **2017**, *91*, 98–102. [CrossRef]
27. Yao, J.; Zeng, F.; Wang, Q. Photonic Generation of Ultrawideband Signals. *J. Light. Technol.* **2007**, *25*, 3219–3235. [CrossRef]
28. Gao, Y.; Wen, A.; Wu, X.; Wang, Y.; Zhang, H. Efficient Photonic Microwave Mixer with Compensation of the Chromatic Dispersion-Induced Power Fading. *J. Light. Technol.* **2016**, *34*, 3440–3448. [CrossRef]

Disclaimer/Publisher's Note: The statements, opinions and data contained in all publications are solely those of the individual author(s) and contributor(s) and not of MDPI and/or the editor(s). MDPI and/or the editor(s) disclaim responsibility for any injury to people or property resulting from any ideas, methods, instructions or products referred to in the content.